Chemical Science

ROYAL SOCIETY OF CHEMISTRY

EDGE ARTICLE

View Article Online
View Journal

Cite this: DOI: 10.1039/d6sc03191a

All publication charges for this article have been paid for by the Royal Society of Chemistry

Increasing connectivity through self-complementarity enables permanent porosity in a halogen-bonded organic framework

Michael P. Moghadasnia, [a] Hayden A. Evans, [b] Adria S. Hippely, [a] J. Julian Sanchez Hernandez,[a] Madilyn G. Holm,[a] Gemma G. Ponce,[a] Hannah R. Martin, [a] Ronin P. Mannina,[a] Brian J. Eckstein,[a] Ryan A. Klein, [b] Praveen Kumar, [c] Charlotte L. Stern,[d] Chris Malliakas, [d] Craig M. Brown [b] and C. Michael McGuirk [*a]

Halogen bonding has emerged as an intuitive and programmable handle for constructing ordered, low-density molecular solids. However, its ability to support permanent porosity has not been realized. Here, we report a self-complementary strategy that surpasses this long-standing limitation, delivering the first rigorously characterized permanently porous halogen-bonded organic framework (XOF). A threefold-symmetric, 2-iodooxazole-terminated tecton spontaneously assembles into a low-density, crystalline network that remains intact upon complete solvent removal. Permanent porosity is confirmed by N_2 gas adsorption–desorption measurements using at 77 K, and the porous topology was monitored *via* X-ray diffraction. This framework is sustained by π-stacked tectons linked through one-dimensional helical chains of C–I···N halogen bonding, yielding full three-dimensional connectivity. Subtle torsional disorder within these chains can be resolved crystallographically, providing rare insight into molecular-level disorder in highly ordered porous frameworks. For comparison, study of an analogous hydrogen-bonded framework composed of a point-modified tecton found rapid structural reorganization upon solvent exchange, supporting more robust intermolecular connectivity in the halogen-bonded system. This work defines a new upper bound for halogen bonding in materials design, establishing XOFs as a distinct permanently porous materials platform.

Received 16th April 2026
Accepted 3rd June 2026

DOI: 10.1039/d6sc03191a

rsc.li/chemical-science

Introduction

Halogen bonding, a subclass of σ-hole bonding, is a predominantly electrostatically attractive noncovalent interaction between an electrophilic halogen atom and a Lewis base.[1–3] While this electrophilicity is seemingly contrary to traditional perceptions of halogen atoms in organic chemistry, late halogen atoms such as bromine and iodine are highly polarizable and weakly electronegative. Thus, when covalently bound to a strong electron-withdrawing group, an appreciable region of low electron density arises where the largest coefficient of the antibonding σ* orbital is found on the halogen atom (Fig. 1a).[4] This, combined with the high p-orbital contribution to σ and σ* and the presence of two pairs of nonbonding electrons, results in a highly localized region of positive electrostatic potential on the outer surface of the halogen atom along the axis of the covalent σ bond (Fig. 1a). This electrophilic region is now broadly referred to as the "σ-hole".

The attractive interaction of a focused Lewis acidic σ-hole with a Lewis base results in a highly directional noncovalent "halogen bond", commonly approaching linearity with the opposing covalent bond (Fig. 1a). Given this preferred directionality and the modular interaction strengths approaching that of canonical hydrogen bonds, halogen bonding has been established as an intuitive molecular design tool for programming intermolecular recognition (Fig. 1b).[5–7] Indeed, halogen bonding has demonstrated similar efficacy to canonical hydrogen bonding in studies spanning crystal engineering, supramolecular ensembles, and catalysis.[8–13]

Yet, in the realm of crystal engineering, almost all reported halogen-bonded structures are densely packed, incorporate charge-stabilizing counterions from anionic Lewis bases,[14,15] or contain intractable solvates required to template low-density structures,[16] following the apparent pseudo-linear trends of density–energy relationships found in most molecular crystal polymorph families (Fig. 1c).[6] Therefore, halogen bonding, in contrast to hydrogen, covalent, and coordination bonds,

[a]Department of Chemistry, Colorado School of Mines, Golden, Colorado 80401, USA. E-mail: cmmcguirk@mines.edu
[b]Center for Neutron Research, National Institute of Standards and Technology, Gaithersburg, Maryland 20899, USA
[c]Shared Instrument Facility, Colorado School of Mines, Golden, Colorado 80401, USA
[d]Department of Chemistry, Northwestern University, Evanston, Illinois 60208, USA

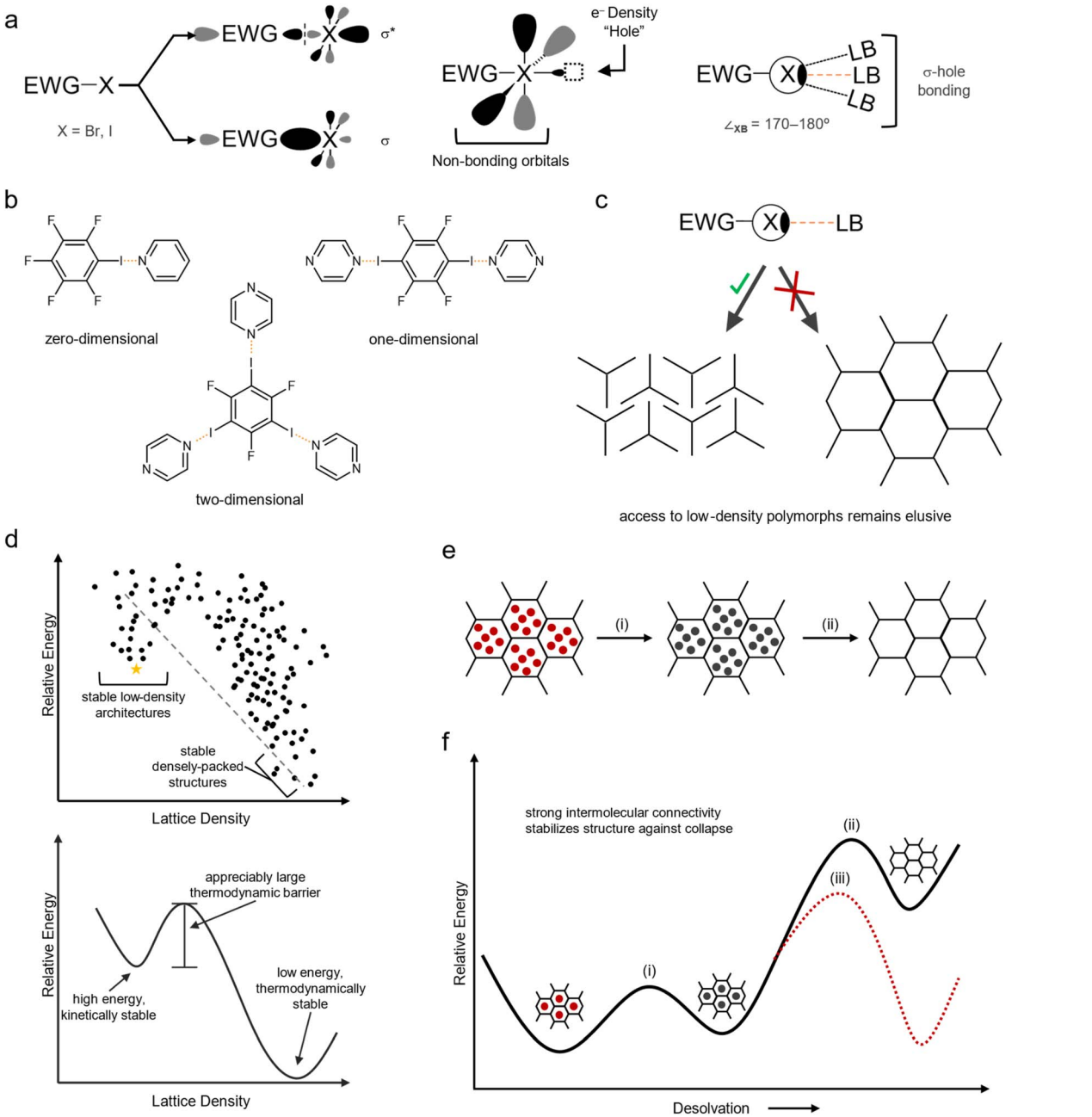

Fig. 1 (a) Graphical representation of a covalent σ bond to a late halogen species (*i.e.*, Br, I) (left) displaying a large coefficient of the σ* outer lobe on the halogen atom. This region of lowered electron density (middle) is conventionally referred to as the σ-hole and additionally focused due to the presence of electron lone pairs. This focused electrophilic region pushes the directionality of halogen bonds with Lewis bases to near linearity (right). (b) Graphical representation of traditional halogen bonding motifs, namely single-point contacts between discrete donor and acceptor species. (c) This common approach to halogen bonding primarily causes formation of densely packed structures rather than low-density or porous crystalline morphologies. (d) Representation of a free energy *vs.* lattice density plot demonstrating the typical relationship and pseudo-linear trend. Stable low-density structures must break this upper bound to exhibit the relative free energy of a denser polymorph. This inversely proportional relationship of energy *vs.* density in materials makes realization of low-density polymorphs a target for demonstrating the upper limit of intermolecular connectivity. (e) Benchmarking porosity in a low-density network requires the ability to (i) completely exchange molecular adsorbates, demonstrating porosity. Permanent porosity requires (ii) the full removal of any adsorbed species (*i.e.*, activation). (f) (i) Solvent exchange and (ii) activation are energy-intensive processes that require strong intermolecular connectivity. Weak connectivity may lead to (iii) collapse into a densely packed phase.

appears fundamentally unable to break this upper bound to assemble kinetically stable, low-density structures in the absence of supporting solvation (Fig. 1c and d). This calls into question the upper limits of halogen bonding and its utility in material design, namely the ability to assemble and stabilize permanently porous materials.

The label of "permanent porosity" is assigned to structurally stable, low-density materials that retain accessible internal surface area upon the removal of molecular adsorbates from the internal void space (Fig. 1e). This accessible void space in permanently porous materials has enabled innumerable applications spanning catalysis,[16] drug delivery,[17] and selective adsorption.[18] However, given the core notion of "horror vacui" (*i.e.*, nature abhors a vacuum), the assembly and stabilization of a kinetically stable, adsorbate-free, and low-density ordered network—far from the global ground state of possible polymorphs—puts great onus on the directionality and strength of the operative mode of intermolecular connectivity (Fig. 1f). As such, the assembly of a low-density network mediated by halogen bonding and retention of long-range structural integrity upon adsorbate removal (*i.e.*, "activation") would provide a clear demonstration of halogen bonding breaking this apparent bound in energy-density crystal packing (Fig. 1d). Furthermore, this would introduce an alternative class of synthetic permanently porous frameworks, the halogen-bonded organic framework (XOF). While examples of low-density networks[19–21] and dynamic porosity[22] exist for halogen bonding systems, as outlined in our recent perspective,[23] the rigorous classification of permanently porous frameworks amongst MOFs, COFs, HOFs—and now XOFs—requires (i) a low-density architecture templated by the designated connectivity in at least two dimensions capable of (ii) retention of long-range structure upon adsorbate exchange and complete removal, and (iii) unambiguous demonstration of porosity *via* gas adsorption–desorption measurements.

With permanent porosity being heavily reliant on stabilization of long-range order through intermolecular connectivity, molecular design is paramount. Traditionally, halogen bonding has leveraged multi-component systems with discrete donor and acceptor molecules designed around optimizing individual halogen bonds. In contrast, we have adopted a new strategy of molecular design that leverages proximal donors and acceptors focused on increasing the density of halogen bonding contacts during supramolecular assembly (Fig. 2a–d). This approach sacrifices the individual strength of halogen bonding contacts to promote stabilization of the extended network.

Here, we report the first conclusive evidence of a permanently porous framework assembled and stabilized by asymmetric halogen bonding. Strategic leveraging of a threefold-symmetric, self-complementary molecular tecton, **B3TFIOx** (Fig. 2e and Scheme 1), resulted in the spontaneous crystallization of a low-density network containing helical one-dimensional C–I···N halogen bonding synthons, giving rise to a three-dimensional halogen-bonded network. Given the non-covalent nature of the intermolecular connectivity, the resulting high crystallinity of the adsorbate-free (*i.e.*, activated) framework enabled atomic-level crystallographic characterization of the structure, including subtle rotational disorder in the halogen-bonded chains. Additional crystallographic and spectroscopic characterization, before and after solvent exchange and removal, supports retention of framework structure and stability through full activation. Isothermal N_2 adsorption–desorption measurements performed at 77 K of the desolvated framework and subsequent Brunauer–Emmett–Teller (BET) analysis confirm the accessible void space of the low-density network with a determined surface area (SA_{BET}) over 750 m^2 g^{-1}. Critically, this ensemble characterization meets the rigorous standards for evidencing claims of permanent porosity and thus makes this the first thoroughly supported demonstration of a permanently porous halogen-bonded organic framework.[24]

Results and discussion

The energy landscape challenge of permanently porous materials

The challenge of realizing permanent porosity in crystalline materials largely stems from the intrinsic relationship between density and energy. Namely, low-density crystalline networks are inherently high in energy relative to densely-packed ground states (Fig. 1d) and are therefore generally stabilized by exothermic interactions with solvent upon assembly (Fig. 1f).[25,26] For a solvated, low-density network to be classified as a porous framework (*i.e.*, not yet permanently porous), demonstration of void space permeability *via* complete guest exchange without long-range structural collapse is required by definition and is proven through combined spectroscopy and diffraction experiments (Fig. 1e).[27] Yet for activation, these same exothermic solvent–surface interactions that lower the overall lattice energy must be overcome through some mode of energetic input (*e.g.*, heat, reduced pressure) to remove the adsorbed solvent and access the lattice void space (Fig. 1f). Additionally, lattice energy intrinsically increases as solvent–surface interactions are weakened, as exemplified when exchanging from *N*,*N*-dimethylformamide (DMF) for *n*-pentane, resulting in a shallower thermodynamic well and greater propensity for rearrangement or collapse (Fig. 1f).[28]

Going a step further, to achieve unambiguous "permanent porosity", a material must maintain its low-density structure with molecularly accessible void space during and after complete removal of adsorbed species. This ensures that only the intermolecular connectivity between building blocks is responsible for producing an appreciably deep local thermodynamic well, while also typically being high in energy relative to the global ground state (Fig. 1d).[27,29,30] Experimentally, supporting complete guest removal and structural integrity with accessible void space requires a combination of NMR spectroscopy, X-ray diffraction, and isothermal gas adsorption–desorption measurements, preferably with N_2 or Ar at their respective boiling points.

Despite decades of study, nearly all halogen-bonded arrays are densely packed with negligible accessible void space. This apparent limitation of halogen bonding is partly due to pervasive strategies for achieving highly negative enthalpies of interaction.[28] Namely, these strategies focus on optimizing the donor (*i.e.*, Lewis acidity) and acceptor (*i.e.*, Lewis basicity) strength of discrete complementary molecules or the use of charged species as donors or acceptors (Fig. 1b).[8,31] However, the reliance on single-point interactions between multiple molecular species or introduction of charged Lewis acids or

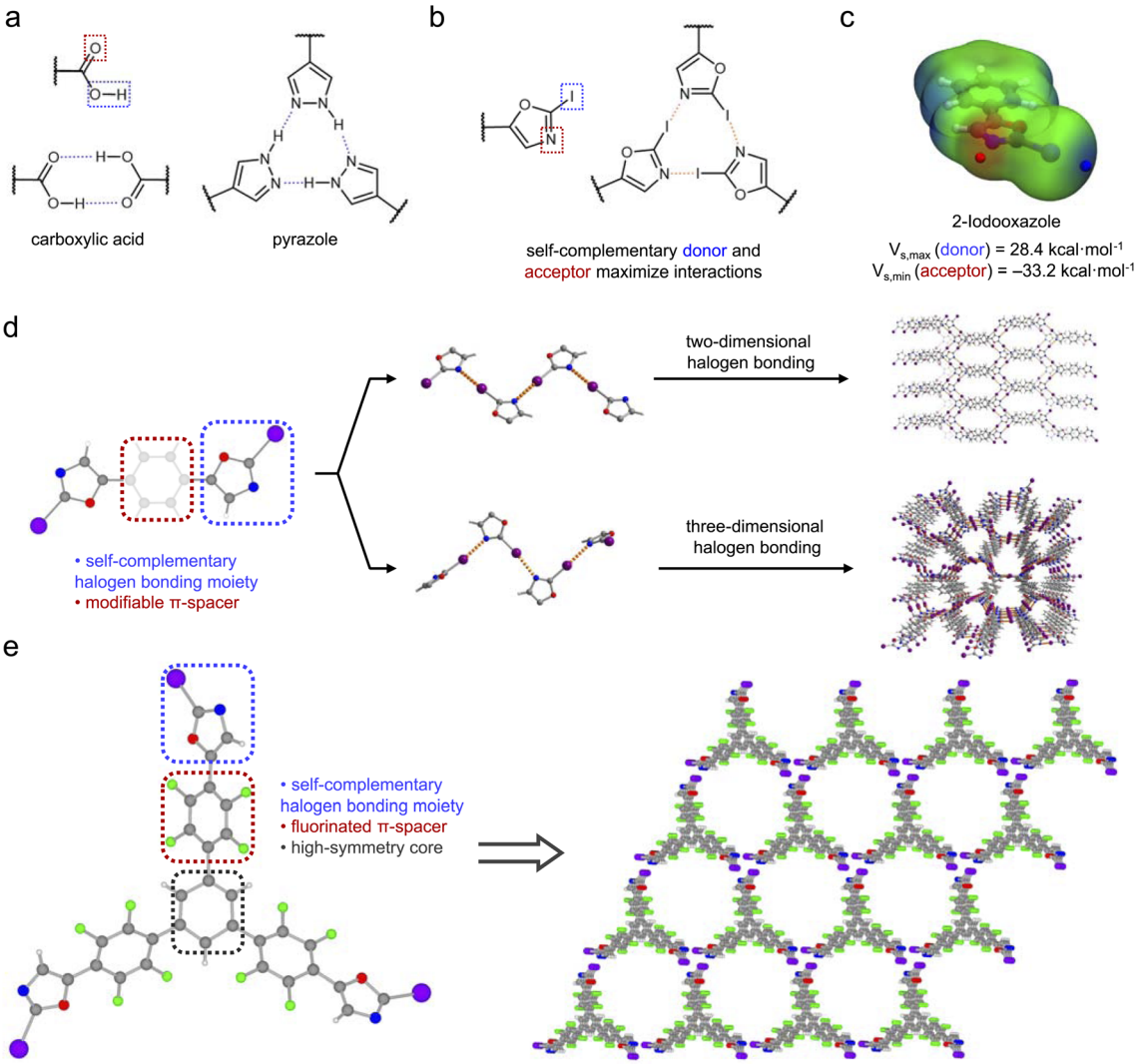

Fig. 2 (a) Self-complementary hydrogen bonding moieties, carboxylic acid (left) and pyrazole (right). (b) Utilizing proximal donor and acceptor species, such as the 2-iodooxazole motif, promotes the assembly of cyclic halogen bonding synthons. (c) DFT-based analysis supports that the 2-iodooxazole motif exhibits desirable surface electrostatic potentials on both the donor (iodine) and acceptor (nitrogen) species. (d) Previous work demonstrates that a linear, twofold halogen bonding tecton is capable of multidimensional assembly of halogen-bonded networks. (e) In this work, targeted assembly of stable, low-density structures is enabled by installation of 2-iodooxazole on a high-symmetry, threefold tecton.

bases greatly complicates the spontaneous assembly of a targeted low-density polymorph with accessible void space and structural integrity, including the need for structure-supporting solvents or counterions within the lattice.

Accordingly, there has yet to be a rigorously characterized example of permanent porosity in a low-density network with halogen bonding in two or more dimensions. The closest examples of demonstrable permanent porosity in a halogen-bonded system come from Maji who report complete desolvation of THF-grown single-crystals in a halogen-bonded molecular crystal. However, isothermal gas adsorption measurements show minimal uptake of N_2 at 77 K and a negligible SA_{BET} of ~9 m^2 g^{-1}, which is consistent with just the external surface adsorption of the crystallite rather than being any evidence of permanent porosity.[32] Additionally, Soldatova report a zwitterionic porous framework assembled through iodonium-based halogen bonds with demonstrable solvent adsorption. However, this system also shows minimal uptake of N_2 at 77 K, exhibiting a calculated SA_{BET} of 17 m^2 g^{-1}.[33] As such, permanently porous frameworks assembled and stabilized through halogen bonding remain elusive.

Self-complementary design strategy

While individual noncovalent interactions are generally considered weak compared to covalent bonding or metal coordination, complementary ensembles of noncovalent interactions can dramatically increase the thermodynamic (*i.e.*, ground state energy) and kinetic (*i.e.*, well depth) stability of a low-density architecture.[34–36] For example, leveraging self-complementary moieties with proximal donor and acceptor groups such as carboxylic acids, pyrazoles, and 3,5-diaminotriazines, has enabled a large family of permanently

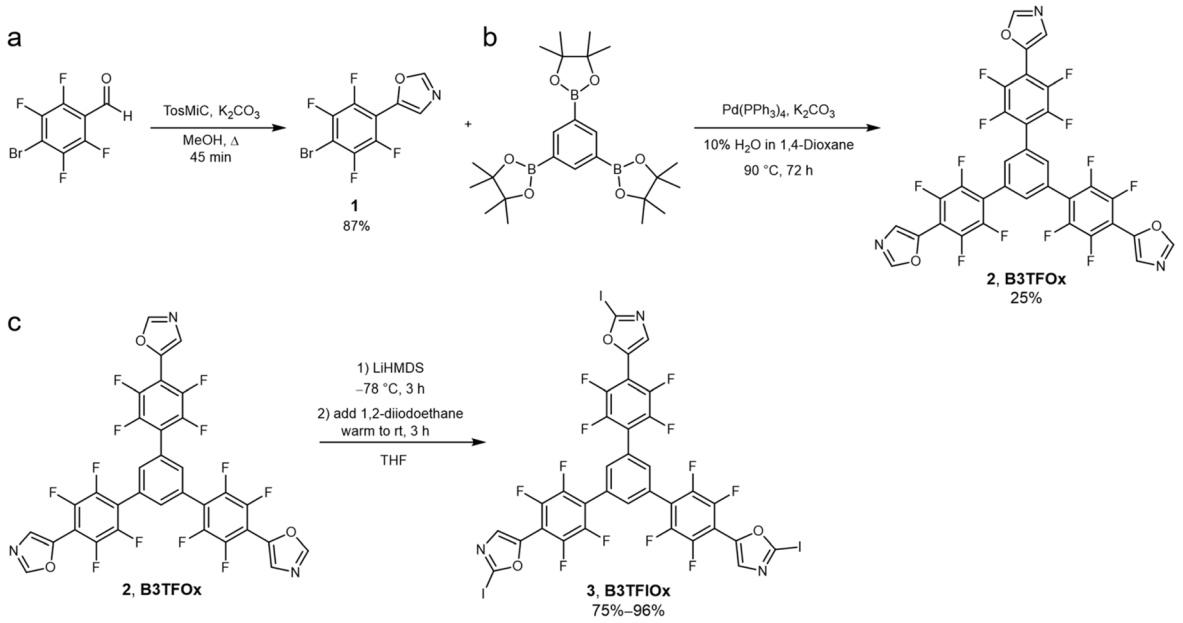

Scheme 1 (a) Oxazole ring formation following the van Leusen synthesis. This step installs the targeted terminal heterocycle while acting as a protecting group for subsequent reactions. (b) Pd-catalyzed Suzuki–Miyaura reaction installs the oxazole-terminated molecular arm onto the central benzene scaffold to form **2**. (c) Lastly, a one-pot, regioselective lithiation allows for the iodination of the oxazole moiety in the 2-position to form **3**.

porous frameworks assembled and stabilized by hydrogen bonding (Fig. 2a).[37–39] Early work by Wuest demonstrates that the rational design of symmetric building blocks (*i.e.*, tectons) functionalized with self-complementary motifs containing proximal donor and acceptor moieties effects robust supramolecular assembly through molecular recognition.[40,41] The evolution of permanently porous hydrogen-bonded organic frameworks has largely been rooted in the design of self-complementary tectons that maximize the number of contacts at intermolecular junctions (*i.e.*, supramolecular synthons) within a lattice, thus increasing the overall connective strength between building blocks (Fig. 2a). We therefore adopted the strategy that self-complementarity was the key to realizing halogen bond-mediated permanent porosity (Fig. 2b).

Rational design of a self-complementary halogen bonding tecton

Given the prior emphasis on optimizing independent donor and/or acceptor molecules in halogen bond-based crystal engineering, self-complementary halogen bonding motifs are rare.[42,43] Therefore, our initial efforts focused on identifying synthetically tractable motifs that exhibited proximal strong donor and acceptor moieties. Computational examination of a series of heterocycles identified 2-iodooxazole as a particularly promising candidate.[35] This novel iodinated heterocycle stood out due to its electrostatic surface potential (ESP) distribution and values, synthetic tractability, and the relatively robust C–I covalent bond, as compared to more labile N–I bonds. The generated ESP map of geometry optimized 2-iodo-5-phenyloxazole exhibits large magnitude potential energy minima ($V_{s,min}$) and maxima ($V_{s,max}$) at the Lewis basic nitrogen acceptor and Lewis acidic iodine donor, respectively, suggesting an appreciable electrostatic driving force for the formation of C–I···N interactions (Fig. 2c).

Subsequent experimental study confirmed that the 2-iodooxazole motif, when functionalized onto a twofold, linear (perfluoro)benzene molecular scaffold, spontaneously assembles into crystalline arrays through self-complementary halogen bonding interactions (Fig. 2d).[35] Additionally, the formation of self-complementary 1D ribbons and local oligomeric synthons assembled through C–I···N contacts could be regulated through consideration of solvent–tecton interactions. These synthon motifs provide a high density of local and long-range 2D and 3D halogen bonding connectivity. However, the observed structures were either appreciably dense or strongly solvated, both precluding observation of (permanent) porosity.

Therefore, to probe if halogen bonding can indeed assemble and stabilize a permanently porous architecture, we hypothesized that a 2-iodooxazole-functionalized tecton with increased molecular symmetry and extended molecular "arms" could assemble a low-density network connected through a high density of intermolecular C–I···N contacts. In turn, this would allow us to determine whether self-complementary halogen bonding provides the requisite thermodynamic and kinetic stability to achieve permanent porosity.

Here, we report the tecton, 1,3,5-tris[2-iodooxazol-5-yl-(2,3,5,6-tetrafluorophenyl)]benzene (**B3TFIOx**, **3**), designed with three core principles in mind (Fig. 2e). First, the proclivity of the 2-iodooxazole moiety for self-association leads to the formation of greater degree of intermolecular halogen bonding contacts. Second, the threefold nature of the 1,3,5-substituted benzene core is amenable to either trimeric or one-dimensional

synthons in a low-density, honeycomb-like topology.[38,39] Third, *para*-substituted 2,3,5,6-tetrafluorophenylene spacers facilitate greater spacing between the tecton core and synthon, and enable stronger π-type (*i.e.*, C–F···π-hole) interlayer stacking. Additionally, the strong electron-withdrawing effect of the fluorinated spacer adjacent to the 2-iodooxazole moiety results in a greater positive electrostatic potential at the $V_{s,max}$ on the iodine atoms. Here, we show that these combined strategies in **B3TFIOx** enable the first demonstration of a permanently porous halogen-bonded organic framework.

Synthesis, crystallization, and network structure

B3TFIOx was synthesized in a convergent, three-step synthesis *via*: (i) oxazole formation,[44,45] (ii) C–C coupling *via* a Pd-catalyzed Suzuki–Miyaura reaction,[46] and (iii) iodination of the 1,3-oxazole moiety (Scheme 1).[47] Of note, we have found that by first installing the 1,3-oxazole moiety at the aldehyde position of 4-bromo-2,3,5,6-tetrafluorobenzaldehyde, the heterocycle serves as an effective protecting group for subsequent cross-coupling with the arene core to form **B3TFOx** (**2**). This allows us to minimize the synthetic steps relative to reported Suzuki couplings with the benzaldehyde moiety.[48] Upon iodination, ^{1}H, ^{13}C, and ^{19}F NMR spectroscopy and subsequent single-crystal X-ray diffraction (SCXRD) analysis support the successful synthesis and purity of **B3TFIOx**.

Hot recrystallization of **B3TFIOx** from solutions of various weakly polar solvents, such as chloroform, carbon tetrachloride, and 1,2-dichlorobenzene, yielded an observably crystalline powdered precipitate (Fig. 3a). Structural analysis of the precipitate obtained upon crystallization from low-boiling point chloroform ($CHCl_3$, b_p = 61 °C) by powder X-ray diffraction (PXRD) revealed a highly crystalline material with reflections below 10° 2θ (λ = 1.5418 Å) often exhibited by honeycomb-like porous framework materials, providing initial support for the assembly of a low-density network, from here on called **B3TFIOx**-I (Fig. 3a).[26,49–51]

We made significant efforts to grow **B3TFIOx**-I crystals of sufficient size and quality for analysis by SCXRD from chloroform and the other solvents that had produced polycrystalline powders with similar diffraction patterns (Fig. S18). However, high-quality single crystals could only be obtained from high-boiling 1-chloronaphthalene (CN, b_p = 263 °C), which revealed a second low-density polymorph by SCXRD that exhibits an overall similar simulated and experimental PXRD pattern to **B3TFIOx**-I (Fig. 3a and S13–S16).

This second polymorph, here called **B3TFIOx**-II, exhibits a twofold interpenetrated, honeycomb-like, low-density structure. Surprisingly, **B3TFIOx**-II exhibits neither coplanar 1D chains nor isolated cyclic oligomers. Rather, an effective averaging of these two previously observed synthons leads to the formation of helical 1D chains with an internal threefold screw axis along the pore direction (Fig. 3b). Notably, the respective networks exhibit opposing left- and right-hand rotational axes in the helical chains parallel to the continuous 1D void space (Fig. 3c). While this structure exhibits a low-density crystalline morphology, any attempts to exchange the 1-chloronaphthalene crystallization solvent resulted in rearrangement into a new crystalline phase (Fig. 3a).

Fortuitously, the rearrangement of **B3TFIOx**-II upon exchange of 1-chloronaphthalene to a less strongly adsorbing solvent, such as *n*-pentane, gave rise to PXRD patterns that were consistent with that of **B3TFIOx**-I grown in chloroform, carbon tetrachloride, and 1,2-dichlorobenzene. This observation leads us to believe that **B3TFIOx**-II is likely a solvate of 1-chloronaphthalene, and exchange to less stabilizing solvents results in spontaneous rearrangement to a more intrinsically stable structure, **B3TFIOx**-I. While growth of high-quality crystals of **B3TFIOx**-I continued to be elusive, the strong correlation between the reflection near ∼4.8° 2θ for **B3TFIOx**-II and a similar reflection for **B3TFIOx**-I (Fig. 3a) arising from the 1D pore width, encouraged us to explore the potential porosity and permanent porosity of the apparently more stable **B3TFIOx**-I.

Solvent exchange, removal, and activated structure determination

To probe the accessibility of the predicted 1D channels of **B3TFIOx**-I, we subjected the chloroform-solvated polycrystalline powder to systematic solvent exchange into *n*-pentane, followed by full solvent removal using supercritical CO_2 ($scCO_2$) activation. Throughout this process, we monitored successful exchange and removal of solvent and retention of the long-range network structure using a combination of PXRD and ^{1}H NMR spectroscopy (Fig. 3d and e). The structure exhibited minimal changes in the measured intensities of the reflections in the powder pattern throughout the exchange process. However, upon full solvent removal *via* $scCO_2$, an apparent broad feature appears in the activated powder around 24–28° 2θ, suggesting the introduction of some new form of disorder (Fig. 3d).[52]

We collected high-resolution synchrotron X-ray powder diffraction (SPXRD) data on the highly crystalline, solvent-free, **B3TFIOx**-I at the Advanced Photon Source at Argonne National Laboratory. By combining the high-quality data from SPXRD with the previously determined structure of **B3TFIOx**-II *via* SCXRD, we obtained a high-confidence, atomic-level model of activated **B3TFIOx**-I through Rietveld refinement (Fig. 4a).

The refinement of desolvated **B3TFIOx**-I reveals the suspected honeycomb-like topology, similar to that observed in **B3TFIOx**-II, assembled through 1D helical halogen bonding motifs and an eclipsed stacking arrangement of the fluorinated spacers along the 1D channel (Fig. 4b and c). The distance of the helical C–I···N contacts vary, with the shortest measurable distance of $d_{C-I\cdots N} \approx 3.1(2)$ Å, which is ≈88% of the summed van der Waals radii (Σr_w). Critically, rather than there being two interpenetrated networks with opposing left- and right-handed helical halogen bonding motifs, **B3TFIOx**-I exhibits a single, converged honeycomb-like network linked by a continuous helical C–I···N halogen bonding motif. Given the high crystallinity of the sample and the use of SPXRD to collect high-quality data, the apparent broadened feature that arises near 24°–28° 2θ (when λ = 1.5418 Å) could be assigned to subtle disorder of

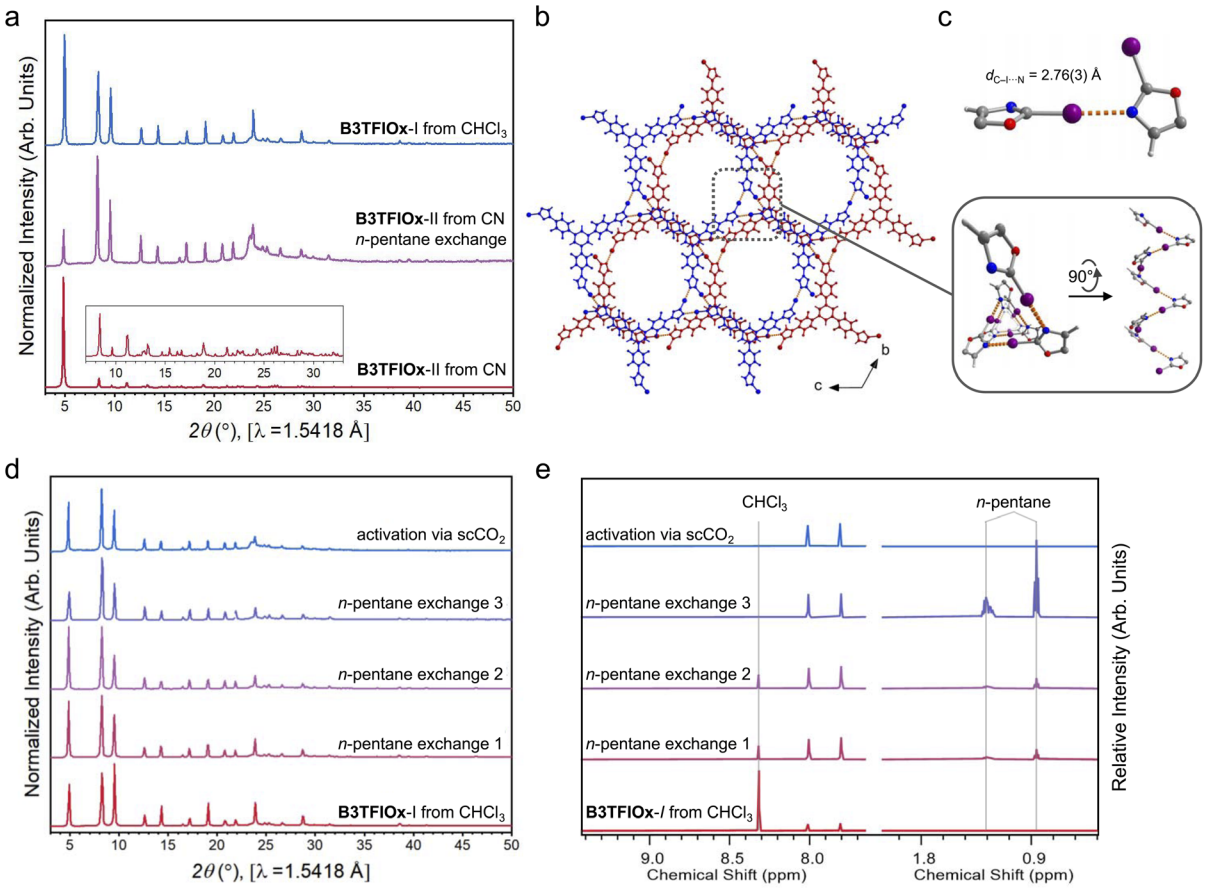

Fig. 3 (a) Crystallization of **B3TFIOx**-I from $CHCl_3$ yielded a highly crystalline powder (blue). Crystallization from 1-chloronaphthalene gave rise to an apparently related, but distinct phase (red), which rearranges to a topology similar to the $CHCl_3$-grown phase upon solvent exchange into *n*-pentane (purple). (b) SCXRD analysis of 1-chloronaphthalene grown **B3TFIOx**-II crystals reveals a twofold interpenetrated, low-density network assembled through helical halogen-bonded oligomers with opposing right- and left-handedness, giving rise to a three-dimensional halogen-bonded network. (c) Callouts provide alternative views of the C–I···N contacts in the one-dimensional helical chains. (d) PXRD and (e) ^{1}H NMR analyses of **B3TFIOx**-I during solvent exchange from chloroform into low-boiling *n*-pentane, followed by solvent removal by $scCO_2$ support retention of long-range structure upon complete solvent removal. Uncertainties reported are ±1 standard deviation.

the oxazole moieties in the halogen-bonded helix (Fig. 4d and e).

This helical disorder is thought to be a result of the small energetic barrier along the axis of rotation in the torsional angle between the fluorinated spacer and the terminal 2-iodooxazole moiety (Fig. S31–S33). DFT-level calculations support this, with the energy barrier of rotation calculated to be less than 4 kcal mol^{-1} (≈16.7 J mol^{-1}). As solvents are exchanged and subsequently removed, energetic input is inevitable. Thus, the disorder in helical halogen bond connectivity is induced during these relatively high energy events needed for full activation of this framework. Nonetheless, the observation and characterization of this low-density network firmly establish the halogen bond-mediated porosity of **B3TFIOx-I**, encouraging us to probe the potential for permanent porosity.

Permanent porosity of B3TFIOx-I

Analysis of the detectably solvent-free **B3TFIOx-I** *via* isothermal equilibrium adsorption–desorption analysis with N_2 at 77 K revealed appreciable adsorption and monolayer formation as low as $P/P_0 = 0.02$, where P and P_0 correspond to the analysis and saturation pressures, respectively ($P_0 = 826$ mbar, elevation of Golden, CO, USA = 1730 m). Adsorption of N_2 begins to reach pore-filling saturation around $P/P_0 = 0.1$, with final uptake capacities reaching ~9 mmol g^{-1} (Fig. 4f). The adsorption profile exhibits canonical Type IV behavior, as defined by IUPAC, with indication of discrete monolayer formation and subsequent pore-filling.[53]

The low relative pressure of the pore-filling event supports the microporous nature of **B3TFIOx-I** observed crystallographically. The BET surface area analysis of **B3TFIOx-I**, using the BETSI software[54] (Fig. S20), estimates an apparent surface area of $SA_{BET} \approx 753$ m^2 g^{-1}. The data density and quality enabled full alignment with the Rouquerol constraints. Calculation of the pore-size distribution using nonlocal density functional theory (NLDFT) from the collected adsorption data indicates ≈13.5 Å-wide pores, consistent with the pore width calculated using PoreBlazer from the refined crystal structure of **B3TFIOx-I** (Fig. S21 and S22). Critically, the PXRD pattern of **B3TFIOx-I** displays structure retention after a series of isothermal

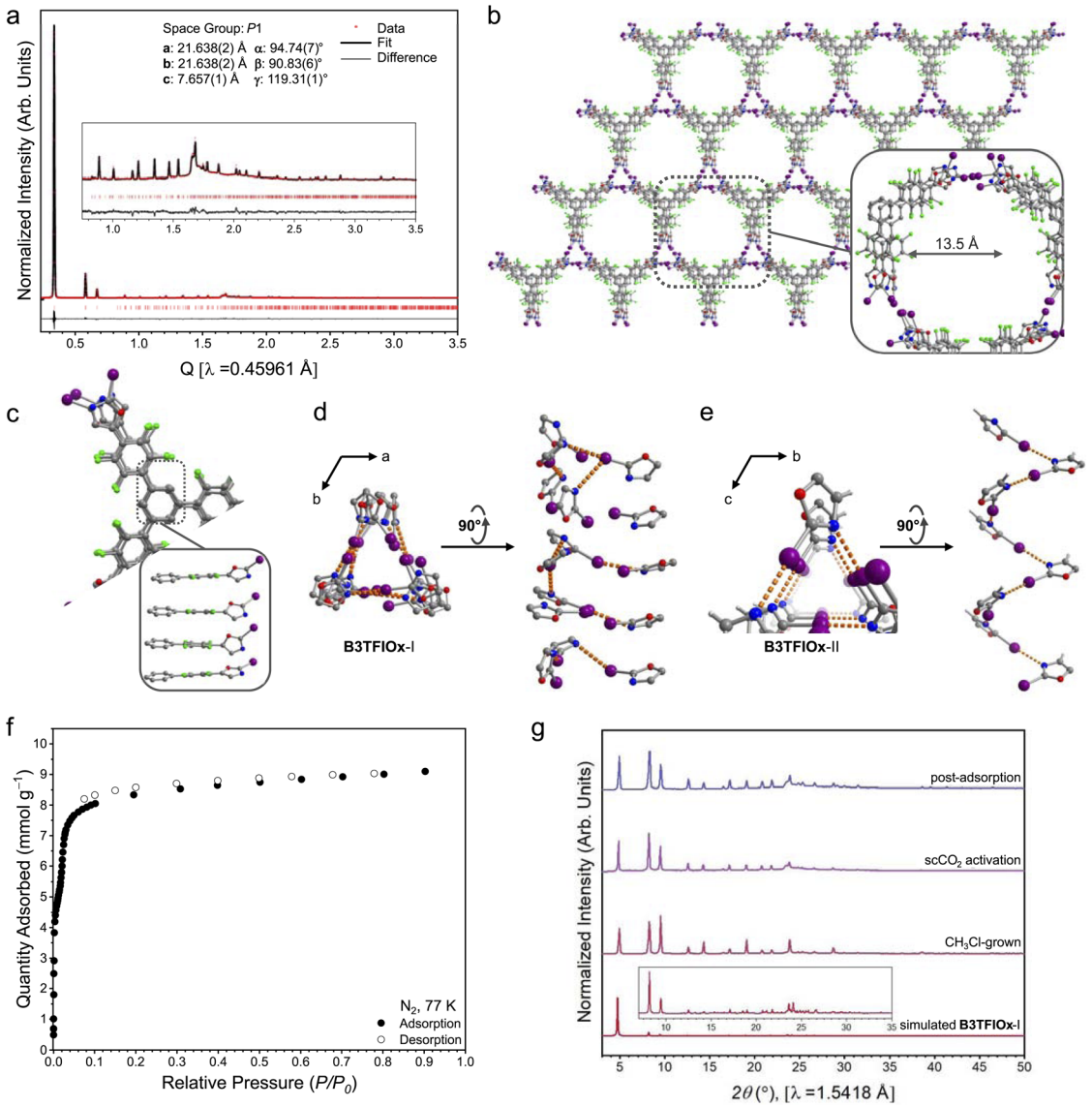

Fig. 4 (a) Following complete solvent removal, the activated **B3TFIOx**-I powder was characterized with SPXRD, providing a structure model in the primitive space group, *P*1, determined *via* Rietveld refinement. A zoomed-in region of the fitted data at higher angles is provided for clarity. (b) Structural analysis reveals a halogen-bonded organic framework with helical C–I···N halogen bonding that assembles into a honeycomb-like topology. (c) **B3TFIOx**-I exhibits nearly eclipsed π-stacking of the perfluorinated spacer. Comparison of the respective helical synthons for (d) **B3TFIOx**-I and (e) **B3TFIOx**-II reveals subtle disorder within the halogen bonding connectivity. (f) A N_2 adsorption–desorption profile collected at 77 K showing over 9 mmol g^{-1} of uptake and a prototypical Type IV profile, indicative of a microporous material.[54] (g) From bottom to top, comparison of the simulated XRD pattern for **B3TFIOx**-I against the experimental PXRD patterns collected for $CHCl_3$-solvated, desolvated, and post-adsorption **B3TFIOx**-I, satisfying the rigorous characterization for permanent porosity. A callout from 7–35° 2θ for the simulated structure is provided for clarity. Uncertainties reported are ±1 standard deviation.

adsorption–desorption measurements, suggesting that the structure is retained throughout the measurements (Fig. 4g). In addition to N_2, other gases were studied (Fig. S25). While weaker adsorbing gases (*e.g.*, H_2, CH_4, and C_2H_6) show uptake capacity less than 1 mmol g^{-1}, strongly adsorbing CO_2 shows a higher uptake capacity of 11 mmol g^{-1}.

With the combination of diffraction-based structural characterization of the as-synthesized and activated material, spectroscopic support for full solvent-removal, BET surface area and pore size analysis *via* N_2 sorption at 77 K, and confirmation of structural integrity after sorption measurements for **B3TFIOx**-I, unequivocal evidence supports our hypothesis that self-complementary halogen bonding can assemble and support a kinetically stable, permanently porous material.

Structural stability of halogen *vs.* hydrogen bonding congeners

We sought to further understand how halogen bonding compares with classical hydrogen bonding in the assembly and stabilization of low-density molecular arrays. Therefore,

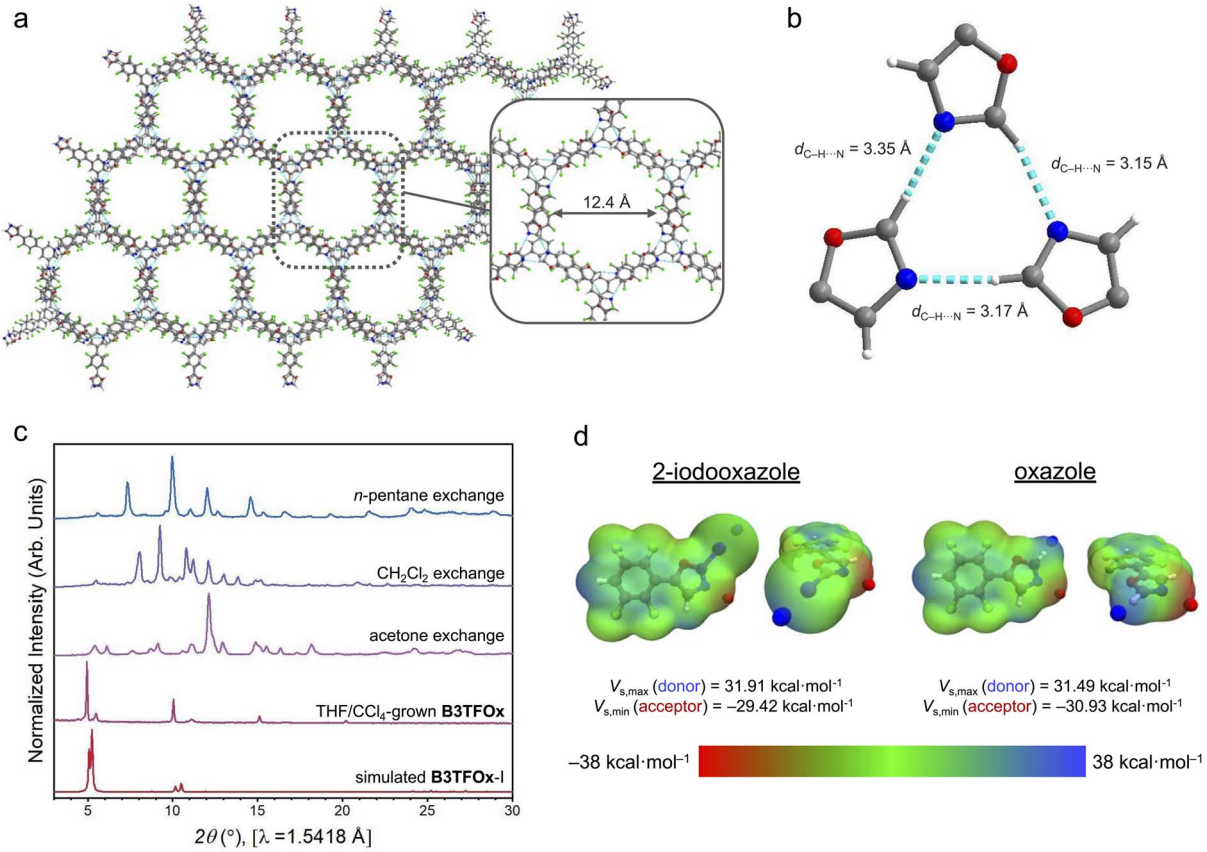

Fig. 5 (a) Portions of the B3TFOx-I crystal grown in 1,4-dioxane revealing an extended honeycomb-like topology. (b) A zoomed-in view of B3TFOx-I which assembles through the oxazole moiety in a cyclic, threefold trimer. Notably, the reported distances, $d_{C-H\cdots N}$, are measured from the experimentally measured carbon and nitrogen atoms only, as the hydrogen atoms were placed during refinement. (c) Attempts to exchange solvent from B3TFOx-I crystals grown in either 1,4-dioxane or 0.05% THF in CCl_4, result in rearrangement. (d) Calculation of the electrostatic surface potential of representative 2,3,5,6-tetrafluorophenyl-2-iodooxazole and 2,3,4,6-tetrafluorophenyloxazole moieties reveals nominal differences in the surface potential of the halogen and hydrogen bonding donor and acceptor moieties. These calculations were performed using the M06-2X/aug-cc-pVTZ level of theory for all hydrogen, carbon, nitrogen, and oxygen atoms while the M06-2X/aug-cc-pVTZ-PP level of theory was used for all iodine atoms. Solvent molecules in panels (a) and (b) were removed for clarity.

B3TFOx (**2**, Scheme 1), the precursor to **B3TFIOx** that contains a polarized C–H bond rather than C–I, was investigated for its potential to self-assemble into a low-density permeable and/or permanently porous framework.

Hot recrystallization of **B3TFOx** in 1,4-dioxane afforded colorless prisms suitable for SCXRD. The structure solution and refinement of these crystals revealed the assembly of **B3TFOx** in a honeycomb-like topology, here called **B3TFOx-I** (Fig. 5a). Unlike the helical threefold synthon present in **B3TFIOx-I** or -II, the isolated, low-density hydrogen-bonded network forms a near-planar, cyclic threefold trimer of C–H···N interactions that extends two-dimensionally (Fig. 5b and S11). Notably, this structure has a similar three-dimensional architecture to the permanently porous, pyrazole-based hydrogen-bonded framework reported by Miljanić.[39] However all attempts for even simple solvent exchange, let alone complete solvent removal, of **B3TFOx-I** result in structural rearrangement into a new crystalline phase (Fig. 5c).

The analyses of both **B3TFOx-I** and the **B3TFIOx-I** and -II crystal structures enable comparison between the halogen- and hydrogen-bonded congeners. Indeed, the rational design of high-symmetry tectons with self-complementary, oxazole-terminated moieties results in the formation of low-density architectures that allow the assembly of one-dimensional channels (Fig. 3b, 4b, and 5a). However, while the non-covalent nature of both hydrogen and halogen bonding affords similar morphologies, only **B3TFIOx-I** exhibits demonstrable permanent porosity (Fig. 4f). The rearrangement of **B3TFOx-I** during solvent exchange supports that the hydrogen-bonded network sits in a shallower thermodynamic well compared to **B3TFIOx-I**. However, the difference in the electrostatic surface potential at the respective hydrogen and halogen bond donor atoms is nominal (31.5 kcal mol^{-1} and 31.9 kcal mol^{-1}, respectively, Fig. 5d).

Thus, accessibility of the helical arrangement in the halogen-bonded synthon appears to influence the thermodynamic accessibility of permanent porosity. Helical and nonplanar assemblies are not unique to halogen bonding, as many examples in hydrogen bonding exhibit nonplanar arrays.[55,56] However, the diffuse region of positive electrostatic surface potential on hydrogen bond donors provides greater flexibility to the hydrogen bonding synthon with minimal energetic

penalty. On the other hand, significantly more directional halogen bonding interactions require near-linear connectivity to form strong, stabilizing interactions which play a more influential role on the final intermolecular connectivity among the molecular congeners. As such, the greater bonding flexibility of hydrogen bonding appears to lead to lower kinetic barriers for rearrangement to other network topologies of relatively similar energy, whereas the halogen bonding system has higher energy barriers and fewer alternative network structures with comparable energy.

Conclusions

We have herein demonstrated that noncovalent halogen bonding can stabilize permanent porosity. This finding validates that halogen bonding exhibits the necessary directionality and strength to spontaneously assemble molecular building blocks into self-sustaining, kinetically stable, low-density architectures. In doing so, we have provided the first unequivocal example of a distinct class of permanently porous framework materials. This was achieved through a self-complementary design strategy that enables a high degree of exothermic connectivity, thereby providing the stabilization required for successful solvent removal and the observation of permanent porosity. Through this work, the apparent limits in utility and reliability of halogen bonding have been surpassed, revealing significant possibilities in the further exploration of material design through these noncovalent interactions. Further studies will seek to understand the influence of halogen bonding synthons on mechanical material properties, such as stiffness and hardness, as well as the influence of late halogen atoms on photophysical properties such as the heavy atom effect leading to room temperature phosphorescent materials for applications in sensing.[57,58]

Author contributions

M. P. M., B. J. E., and C. M. M. contributed to project design. M. P. M. and C. M. M. wrote the manuscript. A. S. H. and H. R. M. assisted with editing and formatting. M. P. M., A. S. H., J. J. S. H., M. G. H., G. G. P., and R. P. M. carried out the experimentation. M. P. M., A. S. H., and H. R. M. conducted the density functional theory analysis. R. A. K., C. L. S., C. M. and P. K. performed diffraction experiments. C. L. S. and C. M. were responsible for structure solution and refinement of single crystal X-ray diffraction data. H. A. E., R. A. K., and C. M. B. performed structure solution and Rietveld refinement from synchrotron powder X-ray diffraction data.

Conflicts of interest

The authors declare no conflicts of interest.

Data availability

CCDC 2528030, 2528031 and 2545736 contain the supplementary crystallographic data for this paper.[59a–c]

The data supporting this article have been included as part of the supplementary information (SI). Supplementary information: synthetic protocols, NMR spectroscopy, crystallization methods, crystallographic structure determination details, isothermal gas adsorption–desorption, thermal analysis, and computational methods and results. See DOI: https://doi.org/10.1039/d6sc03191a.

Acknowledgements

This work was partially supported by the NSF DMR SSMC (Award #2143623) as well as start-up funds from Colorado School of Mines. H. A. E. and C. M. B. were wholly supported by NIST. This work made use of the IMSERC crystallography facility at Northwestern University as well as beamline 17-BM at the Advanced Photon Source at Argonne National Laboratory. Certain commercial equipment, instrumentation, or materials are identified in this document. Such identification does not imply recommendation or endorsement by the National Institute of Standards and Technology, nor does it imply that the products identified are necessarily the best available for the purpose.

Notes and references

1 G. R. Desiraju, P. S. Ho, L. Kloo, A. C. Legon, R. Marquardt, P. Metrangolo, *et al.*, *Pure Appl. Chem.*, 2013, **85**, 1711–1713.
2 T. Clark, M. Hennemann, J. S. Murray and P. Politzer, *J. Mol. Model.*, 2006, **13**, 291–296.
3 H. A. Evans, J. L. Andrews, D. H. Fabini, M. B. Preefer, G. Wu, A. K. Cheetham, *et al.*, *Chem. Commun.*, 2019, **55**, 588–591.
4 L. P. Wolters and F. M. Bickelhaupt, *ChemistryOpen*, 2012, **1**, 96–105.
5 P. Metrangolo and G. Resnati, *Chem. Eur J.*, 2001, **7**, 2511–2519.
6 X. H. Ding, Y. Z. Chang, C. J. Ou, J. Y. Lin, L. H. Xie and W. Huang, *Natl. Sci. Rev.*, 2020, **7**, 1906–1932.
7 J. N. Smith and N. G. White, *Cryst. Growth Des.*, 2024, **24**, 6771–6779.
8 G. Cavallo, P. Metrangolo, R. Milani, T. Pilati, A. Priimagi, G. Resnati, *et al.*, *Chem. Rev.*, 2016, **116**, 2478–2601.
9 P. J. Costa, *Phys. Sci. Rev.*, 2017, **2**, 20170136.
10 C. Que, Q. Qi, D. Y. Zemlyanov, H. Mo, A. Deac, M. Zeller, *et al.*, *Cryst. Growth Des.*, 2020, **20**, 3224–3235.
11 A. Brown and P. D. Beer, *Chem. Commun.*, 2016, **52**, 8645–8658.
12 R. L. Sutar and S. M. Huber, *ACS Catal.*, 2019, **9**, 9622–9639.
13 N. Juneja, N. M. Shapiro, D. K. Unruh, E. Bosch, R. H. Groeneman and K. M. Hutchins, *Angew. Chem., Int. Ed.*, 2022, **61**, e202202708.
14 X. Bai, Z. Tian, H. Dong, N. Xia, J. Zhao, P. Sun, *et al.*, *Angew. Chem., Int. Ed.*, 2024, **63**, e202408428.
15 J. N. Smith, C. I. Hunter, H. V. Doan, V. P. Ting and N. G. White, *Angew. Chem.*, 2024, **137**, e202422197.
16 R. Tepper and U. S. Schubert, *Angew. Chem., Int. Ed.*, 2018, **57**, 6004–6016.

17 H. Molavi, H. Moghimi and R. A. Taheri, *Appl. Organomet. Chem.*, 2020, **34**, e5549.
18 H. A. Evans, D. Mullangi, Z. Deng, Y. Wang, S. B. Peh, F. Wei, *et al.*, *Sci. Adv.*, 2022, **8**, eade1473.
19 S. Shankar, O. Chovnik, L. J. W. Shimon, M. Lahav and M. E. Van Der Boom, *Cryst. Growth Des.*, 2018, **18**, 1967–1977.
20 Q. Zhao, S. Lin, P. Sun, Y. Lu, Q. Li, Z. Tian, *et al.*, *Adv. Funct. Mater.*, 2025, **35**, 2421755.
21 Q. Jia, C. Zhao, W. Zhu, N. Fang, X. He and Y. Zhao, *Angew. Chem.*, 2025, **137**, e202517907.
22 P. Metrangolo, Y. Carcenac, M. Lahtinen, T. Pilati, K. Rissanen, A. Vij, *et al.*, *Science*, 2009, **323**, 1461–1464.
23 M. P. Moghadasnia, B. J. Eckstein, H. R. Martin, J. U. Paredes and C. M. McGuirk, *Cryst. Growth Des.*, 2024, **24**, 2304–2321.
24 N. G. White and C. M. McGuirk, *Chem. Soc. Rev.*, 2025, 9612–9629.
25 A. G. Slater and A. I. Cooper, *Science*, 2015, **348**, aaa8075–aaa.
26 A. Pulido, L. Chen, T. Kaczorowski, D. Holden, M. A. Little, S. Y. Chong, *et al.*, *Nature*, 2017, **543**, 657–664.
27 L. J. Barbour, *Chem. Commun.*, 2006, 1163–1168.
28 J. R. H. Manning, G. Donval, M. Tolladay, T. L. Underwood, S. C. Parker and T. Düren, *J. Mater. Chem. A*, 2023, **11**, 25929–25937.
29 I. Hisaki, C. Xin, K. Takahashi and T. Nakamura, *Angew. Chem., Int. Ed.*, 2019, **58**, 11160–11170.
30 X. Zhang, Z. Chen, X. Liu, S. L. Hanna, X. Wang, R. Taheri-Ledari, *et al.*, *Chem. Soc. Rev.*, 2020, **49**, 7406–7427.
31 A. Priimagi, G. Cavallo, P. Metrangolo and G. Resnati, *Acc. Chem. Res.*, 2013, **46**, 2686–2695.
32 S. Maji and R. Natarajan, *Small*, 2023, **19**, 2302902.
33 N. S. Soldatova, P. S. Postnikov, D. M. Ivanov, O. V. Semyonov, O. S. Kukurina, O. Guselnikova, *et al.*, *Chem. Sci.*, 2022, **13**, 5650–5658.
34 K. Raatikainen and K. Rissanen, *Chem. Sci.*, 2012, **3**, 1235–1239.
35 M. P. Moghadasnia, B. J. Eckstein, G. J. Balaich and C. M. McGuirk, *Cryst. Growth Des.*, 2023, **23**, 5066–5073.
36 B. J. Eckstein, H. R. Martin, M. P. Moghadasnia, A. Halder, M. J. Melville, T. N. Buzinski, *et al.*, *Chem. Commun.*, 2024, **60**, 758–761.
37 X. Song, Y. Wang, C. Wang, D. Wang, G. Zhuang, K. O. Kirlikovali, *et al.*, *J. Am. Chem. Soc.*, 2022, **144**, 10663–10687.
38 M. I. Hashim, H. T. M. M. Le, T.-H. H. Chen, Y.-S. S. Chen, O. Daugulis, *et al.*, *J. Am. Chem. Soc.*, 2018, **140**, 6014–6026.
39 T.-H. Chen, I. Popov, W. Kaveevivitchai, Y.-C. Chuang, Y.-S. Chen, O. Daugulis, *et al.*, *Nat. Commun.*, 2014, **5**, 5131.
40 J. D. Wuest, *Chem. Commun.*, 2005, 5830–5837.
41 M. Simard, D. Su and J. D. Wuest, *J. Am. Chem. Soc.*, 1991, **113**, 4696–4698.
42 T. Mukai and K. Nishikawa, *X-Ray Struct. Anal. Online*, 2013, **29**, 13–14.
43 P. M. J. Szell, A. Siiskonen, L. Catalano, G. Cavallo, G. Terraneo, A. Priimagi, *et al.*, *New J. Chem.*, 2018, **42**, 10467–10471.
44 A. M. Van Leusen, B. E. Hoogenboom and H. Siderius, *Tetrahedron Lett.*, 1972, **13**, 2369–2372.
45 S. Kotha and V. R. Shah, *Synthesis*, 2007, 3653–3658.
46 N. Miyaura and A. Suzuki, *Chem. Rev.*, 1995, **95**, 2457–2483.
47 E. Vedejs and L. M. Luchetta, *J. Org. Chem.*, 1999, **64**, 1011–1014.
48 W. A. Braunecker, K. E. Hurst, K. G. Ray, Z. R. Owczarczyk, M. B. Martinez, N. Leick, *et al.*, *Cryst. Growth Des.*, 2018, **18**, 4160–4166.
49 B. J. Eckstein, L. C. Brown, B. C. Noll, M. P. Moghadasnia, G. J. Balaich and C. M. McGuirk, *J. Am. Chem. Soc.*, 2021, **143**, 20207–20215.
50 L. A. Baldwin, J. W. Crowe, M. D. Shannon, C. P. Jaroniec and P. L. McGrier, *Chem. Mater.*, 2015, **27**, 6169–6172.
51 J.-H. Dou, M. Q. Arguilla, Y. Luo, J. Li, W. Zhang, L. Sun, *et al.*, *Nat. Mater.*, 2021, **20**, 222–228.
52 E. Sebti, H. A. Evans, H. Chen, P. M. Richardson, K. M. White, R. Giovine, *et al.*, *J. Am. Chem. Soc.*, 2022, **144**, 5795–5811.
53 M. Thommes, K. Kaneko, A. V. Neimark, J. P. Olivier, F. Rodriguez-Reinoso, J. Rouquerol, *et al.*, *Pure Appl. Chem.*, 2015, **87**, 1051–1069.
54 BETSI-GUI, https://github.com/nakulrampal/betsi-gui, (accessed 2025).
55 J. Huang, Y. Li, H. Zhang, Z. Yuan, S. Xiang, B. Chen, *et al.*, *Angew. Chem., Int. Ed.*, 2023, **62**, e202315987.
56 I. A. Baburin, V. A. Blatov, L. Carlucci, G. Ciani and D. M. Proserpio, *Cryst. Growth Des.*, 2008, **8**, 519–539.
57 W. Wang, Y. Zhang and W. J. Jin, *Coord. Chem. Rev.*, 2020, **404**, 213107.
58 S. Hirata, *Adv. Opt. Mater.*, 2017, **5**, 1700116.
59 (*a*) CCDC 2528030: Experimental Crystal Structure Determination, 2026, DOI: 10.5517/ccdc.csd.cc2qvmcl; (*b*) CCDC 2528031: Experimental Crystal Structure Determination, 2026, DOI: 10.5517/ccdc.csd.cc2qvmdm; (*c*) CCDC 2545736: Experimental Crystal Structure Determination, 2026, DOI: 10.5517/ccdc.csd.cc2rg1jt.